Superconducting transmon qubits with niobium-buffered α-tantalum on sapphire substrates

Tingting Guo(郭婷婷), Zishuo Li(李子硕), Lili Shi(石粒力), Junliang Jiang(江俊良), Yifan Sheng(盛怡凡), Wenqu Xu(许问渠), Lingxiao Jing(景凌啸), Binglin Li(李柄霖), Kaixuan Zhang(张凯旋), Tianshi Zhou(周天石), Chunhai Cao(曹春海), Guozhu Sun(孙国柱), Peiheng Wu(吴培亨)

Citation: Chin. Phys. B. 35, 108503 (2026). DOI: 10.1088/1674-1056/ae23af | CSTR: 32038.14.CPB.ae23af
http://cpb.iphy.ac.cn; http://iopscience.iop.org/cpb

What follows is a list of articles you may be interested in

Optimize Purcell filter design for reducing influence of fabrication variation

Xiao Cai(蔡晓), Yi-Biao Zhou(周翼彪), Wen-Long Yu(于文龙), Kang-Lin Xiong(熊康林), Jia-Gui Feng(冯加贵)

Chin. Phys. B. 33, 068501 (2024). DOI: 10.1088/1674-1056/ad3345

Terahertz high-sensitivity SIS mixer based on Nb–AlN–NbN hybrid superconducting tunnel junctions

Bo-Liang Liu(刘博梁), Dong Liu(刘冬), Ming Yao(姚明), Jun-Da Jin(金骏达), Zheng Wang(王争), Jing Li(李婧), Sheng-Cai Shi(史生才), Artem Chekushkin, Michael Fominsky, Lyudmila Filippenko, Valery Koshelets

Chin. Phys. B. 33, 058501 (2024). DOI: 10.1088/1674-1056/ad2bf7

Fabrication and characterization of all-Nb lumped-element Josephson parametric amplifiers

Hang Xue(薛航), Zhirong Lin(林志荣), Wenbing Jiang(江文兵), Zhengqi Niu(牛铮琦), Kuang Liu(刘匡), Wei Peng(彭炜), Zhen Wang(王镇)

Chin. Phys. B. 30, 068503 (2021). DOI: 10.1088/1674-1056/abeee6

Room-temperature electric control of exchange bias effect in $CoO_{1-\delta}$/Co films using $Pb(Mg_{1/3}Nb_{2/3})_{0.7}Ti_{0.3}O_3$ (110) substrates

Xin Wen(闻馨), Rui Wu(吴锐), Wen-Yun Yang(杨文云), Chang-Sheng Wang(王常生), Shun-Quan Liu(刘顺荃), Jing-Zhi Han(韩景智), Jin-Bo Yang(杨金波)

Chin. Phys. B. 29, 098503 (2020). DOI: 10.1088/1674-1056/aba611

Wavelength dependence of intrinsic detection efficiency of NbN superconducting nanowire single-photon detector

Yong Wang(王勇), Hao Li(李浩), Li-Xing You(尤立星), Chao-Lin Lv(吕超林), He-Qing Wang(王河清), Xing-Yu Zhang(张兴雨), Wei-Jun Zhang(张伟君), Hui Zhou(周慧), Lu Zhang(张露), Xiao-Yan Yang(杨晓燕), Zhen Wang(王镇)

Chin. Phys. B. 28, 078502 (2019). DOI: 10.1088/1674-1056/28/7/078502

Superconducting transmon qubits with niobium-buffered α-tantalum on sapphire substrates

Tingting Guo(郭婷婷)[1,2,3,†], Zishuo Li(李子硕)[1,2,3,†], Lili Shi(石粒力)[1,2,3], Junliang Jiang(江俊良)[1,2,3], Yifan Sheng(盛怡凡)[1,2,3], Wenqu Xu(许问渠)[1,2,3], Lingxiao Jing(景凌啸)[1,2,3], Binglin Li(李柄霖)[1,2,3], Kaixuan Zhang(张凯旋)[1,2,3], Tianshi Zhou(周天石)[1,2,3], Chunhai Cao(曹春海)[1,3], Guozhu Sun(孙国柱)[1,2,3,4,‡], and Peiheng Wu(吴培亨)[1,2,3]

[1] *Research Institute of Superconductor Electronics, School of Electronic Science and Engineering, Nanjing University, Nanjing* 210023, *China*
[2] *Purple Mountain Laboratories, Nanjing* 211111, *China*
[3] *Hefei National Laboratory, Hefei* 230088, *China*
[4] *Shishan Laboratory, Suzhou Campus of Nanjing University, Suzhou* 215163, *China*

(Received 27 September 2025; revised manuscript received 12 November 2025; accepted manuscript online 25 November 2025)

Tantalum (Ta) is a promising material for superconducting qubits due to its stable chemical properties, formation of a single oxide, and resistance to reaction with other substances. However, achieving the desired α-Ta typically requires high-temperature substrate heating, leading to a time-consuming process and stringent requirements for the film deposition system. Here we demonstrate the deposition of high-quality α-Ta at room temperature using a niobium (Nb) film as a buffer layer. The buffered films are characterized using x-ray diffraction, transmission electron microscopy, and scanning electron microscopy. Transmons with capacitors, transmission lines, and readout resonators fabricated with such Nb-buffered Ta exhibit excellent performance. We observed an "inflection point" in the dependence of the Q_i of the resonators on the input microwave photons, which can be fitted well with an expression for the superposition of the buffered resonators. These experimental results show that the buffered films deposited at room temperature have promising applications in superconducting devices.

Keywords: Nb-buffered, tantalum, superconducting qubit, resonator

PACS: 85.25.Cp

DOI: 10.1088/1674-1056/ae23af **CSTR:** 32038.14.CPB.ae23af

1. Introduction

Superconducting qubits are among the most promising platforms for quantum computing. Significant improvements in qubit coherence times have been achieved through the optimization of circuit design, material selection, and fabrication processes.[1–15] Materials such as niobium (Nb), aluminum (Al), niobium nitride (NbN), titanium nitride (TiN), and niobium titanium nitride (NbTiN) are commonly used in the peripheral circuits of superconducting qubits. Major sources of two-level systems (TLSs) are the presence of defects in the crystal lattice and on the interface and/or surface of materials. The energy difference of these defects is close to that of the qubit, which induces the decoherence of the qubit.[16] Recently, α-phase tantalum (Ta) films have garnered increasing attention due to their superior performance. Superconducting qubits based on α-phase Ta films exhibit significantly enhanced coherence times,[12–14] which is mainly attributed to the lower microwave loss of tantalum oxide compared to traditional materials such as Nb and Al. Additionally, Ta's chemical stability and resistance to reactivity facilitate the multi-step cleaning processes, making it an ideal material for superconducting qubits.

Ta may exist in two phases: the α-phase (α-Ta), which has a body-centered cubic (bcc) structure with a lattice constant of 3.306 Å, and the β-phase (β-Ta), which features a tetragonal lattice structure with lattice constants $a = 10.194$ Å and $c = 5.313$ Å. The resistivity of β-Ta is an order of magnitude higher than that of α-Ta, although both α-Ta and β-Ta are superconducting. The critical temperatures (T_c) of bulk α-Ta and β-Ta are 4.48 K and 0.6 K, respectively. β-Ta is typically obtained when the film is deposited at room temperature, whereas α-Ta can be achieved by controlling the argon gas pressure during DC magnetron sputtering.[17,18] Additionally, α-Ta can be obtained through the application of a bias to the substrate during RF sputtering,[19] or via high-power impulse magnetron sputtering combined with the negative bias of the substrate. Vacuum annealing at 700 °C can also assist the transition from β-Ta to α-Ta.[20–22] Although some of these methods allow for the deposition of α-Ta without heating the substrates during sputtering, they often result in the formation of multiple crystal orientations. In order to obtain pure α-Ta, the film growth is typically performed with high-temperature heating. For example, previous studies

[†] These authors contributed equally to this work.
[‡] Corresponding author. E-mail: gzsun@nju.edu.cn

© 2026 Chinese Physical Society and IOP Publishing Ltd. All rights, including for text and data mining, AI training, and similar technologies, are reserved.

have successfully deposited α-Ta films on sapphire substrates using high-temperature techniques.[12–14,23,24] However, the long growth duration associated with high vacuum and the tendency of photoresists to be carbonized at high temperature limit the applicability of α-Ta films in some fabrication processes such as building suspended structures and/or lift-off processes. To reduce the time and cost associated with film growth and enhance the fabrication flexibility, Nb has been introduced as a buffer layer. Nb has a body-centered cubic structure, and its lattice constant matches that of α-Ta with only a 1% mismatch, which promotes the growth and nucleation of α-Ta.[25–27] By depositing a Nb film as the buffer layer, α-Ta has been successfully grown at room temperature,[25,28] and implemented in high coherence quantum circuits. Recently, some researchers have successfully grown α-tantalum films at room temperature without a seed layer. However, this growth window remains relatively narrow.[29] To achieve stable growth of α-tantalum films at room temperature, the introduction of a seed layer remains essential. Here, we demonstrate the implementation of low-loss α-Ta films using Nb as the buffer layer on sapphire substrates in transmon qubits and CPW resonators.

Here, we propose and demonstrate the deposition of low-loss α-Ta films using Nb as the buffer layer on sapphire substrates at room temperature. The buffered films are characterized by x-ray diffraction (XRD), transmission electron microscopy (TEM), and scanning electron microscopy (SEM). We fabricate resonators and transmons with such Nb-buffered α-Ta, which exhibit interesting and excellent performance. In our experiments after one year, we find that although the Q_i of the resonator decreases, the performance of the qubits increases, which is caused mainly by the temperature. Furthermore, we observe an "inflection point" in the dependence of the Q_i of the resonators on the input microwave photons, which can be described by a model including the sum of losses in the buffered films. This may be helpful in understanding the TLS sources in the superconducting resonators and qubits.

2. Results and discussion

2.1. Characterization of the films

Following the methods described in the supplementary information, we deposited the Nb-buffered Ta film and fabricated superconducting resonators and transmon qubits. Several crystal orientations may exist in α-Ta, with the 110 orientation expected to be dominant. The XRD result in logarithmic coordinates (Fig. 1(a)) shows the crystal orientation of the Nb-buffered Ta film. For comparison, the XRD result of a Ta film deposited at room temperature with the same thickness but without the Nb buffer layer is also shown. The latter film exhibits several crystal orientations: (002), (110), and (004), suggesting a mixture of α-phase [(110)] and β-phase [(004) and (002)], which are consistent with the previous results.[25] Figure 1(b) shows the rocking curve for the (110) orientation (highlighted by a purple box in Fig. 1(a)). The presence of the bottom Nb layer improves the matching between the upper Ta film and the sapphire substrate, promoting the growth of α-Ta.

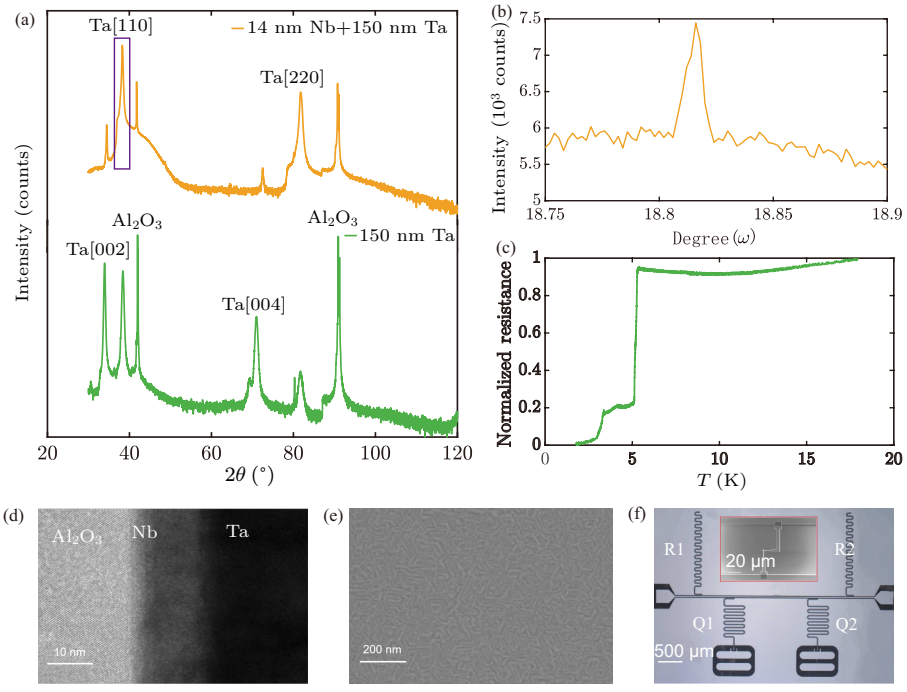

Fig. 1. (a) XRD result for the Ta films with and without a 14-nm Nb buffer layer. (b) Rocking curve around α-phase Ta (110) indicated by the purple box in panel (a). (c) Temperature dependence of the resistivity of the Ta film with a 14-nm Nb buffer layer. The superconducting transition temperatures of the bottom Nb and the upper Ta are about 5.09 K and 2.97 K, respectively. (d) Cross-sectional TEM image of the Nb-buffered Ta film near the sapphire substrate. (e) SEM image of the Nb-buffered Ta film with grains clearly demonstrated. (f) Sample containing two resonators (R1 and R2) and two transmons (Q1 and Q2). The inset shows the SEM image of the area around the Josephson junction.

The resistance versus temperature of the Nb-buffered Ta film is measured, as shown in Fig. 1(c), in a pulse tube refrigerator with the lowest temperature of about 2 K. The size of the measured sample is about 13 mm ×4 mm. Two superconducting critical temperatures (T_c) are observed: one is approximately 5.09 K for Nb, and the other is about 2.97 K for Ta. The T_c of the Ta film is lower than that of its bulk material. Because the sputtering temperature, power, and time during the growth of the Ta film will greatly affect its T_c,[30] the optimization of the growth conditions is promising for improving the T_c of the buffered Ta film. The Nb-buffered Ta film is also characterized using SEM and TEM. Figure 1(d) shows the cross-sectional TEM of the Nb–Ta film. From left to right, the layers are sapphire, Nb, and Ta, respectively. The 14-nm thick Nb buffer layer is clearly evident. The Ta film exhibits a particle size of about 67 nm, and the arrangement and appearance of the grains closely resemble those of high-quality α-Ta films,[12–14,23,27,31] as shown in Fig. 1(e).

2.2. Resonator performance

As shown in Fig. 1(f), two resonators (labeled as R1 and R2) and superconducting transmon qubits (labeled as Q1 and Q2) have been fabricated using Nb-buffered Ta film on the same substrate. Each resonator is a coplanar-waveguide quarter-wavelength one with a central conductor that is 10 μm wide, positioned 5 μm from the ground to ensure a characteristic impedance of 50 Ω. The center conductor of the resonator is 41 μm away from that of the IO line, which yields a coupling coefficient of about 5×10^4. For qubits, a traditional transmon design[12–14] is adopted, in which each Ta pad is 680 μm×150 μm with rounded corners. Such a dumbbell-type capacitor structure has a smaller substrate-metal participation ratio compared to that of the interdigital geometry.[32] The Josephson junction of 170 nm × 170 nm is Manhattan-type, which has a higher yield rate compared to that with Dolan bridges, because the area of the junction does not depend on the evaporation angles and the bridgeless structure will not collapse during the ion milling.

The transmission characteristics of the resonators are shown in the insets of Fig. 2(a) and Fig. 2(b). From these, the internal quality factor Q_i can be deduced by fitting the experimental data with the DCM model.[33,34] The loss sources in the resonator vary with the temperature and photon numbers. Thus Q_i depends on the temperature and input power, which is well described by a model containing three sources of loss: two-level systems (TLS), nonequilibrium quasiparticles (QP), and a power- and temperature-independent loss channel[24,25,35] represented by δ_{TLS}, δ_{QP}, and δ_{other}. However, in our experiment, due to the low and constant temperature during the variation of the input microwave photons, the loss caused by the quasiparticles becomes negligible.[23,36,37] We fit the data with the following model

$$\delta_i = \delta_{TLS} + \delta_{other}, \tag{1}$$

where δ_{TLS} can be rewritten as

$$\delta_{TLS} = \frac{F\delta_{TLS,0}}{\sqrt{1+(\frac{\bar{n}}{C})^{\beta}}}, \tag{2}$$

where $\bar{n}$ is the average number of photons in the resonator and C is the characteristic photon number when TLS is saturated. At the low temperature and with the low input microwave power, the internal loss approaches $F\delta_{TLS,0}$, which is mainly limited by the unsaturated TLS. As the number of input microwave photons increases, Q_i increases as expected, as shown in the results of the first measurement in Fig. 2(a) and Fig. 2(b). Table 1 lists the fitting parameters using Eq. (1). Detailed sample fabrication processes, in which losses may be introduced, are given and analyzed in supplementary information.

Table 1. Fitting parameters of two resonators used in Eq. (1). R1 and R2 represent two resonators, respectively. The errors indicate the standard deviation of the parameter estimation.

Resonator	f_c (GHz)	$F\delta_{TLS,0}$ (10^{-6})	C (10^3)	β	δ_{other} (10^{-6})
R1	7.5393	2.627±0.16	2.895±0.80	0.5±0.06	1.76±0.10
R2	7.6612	2.43±0.26	2.36±1.19	0.37±0.06	1.69±0.15

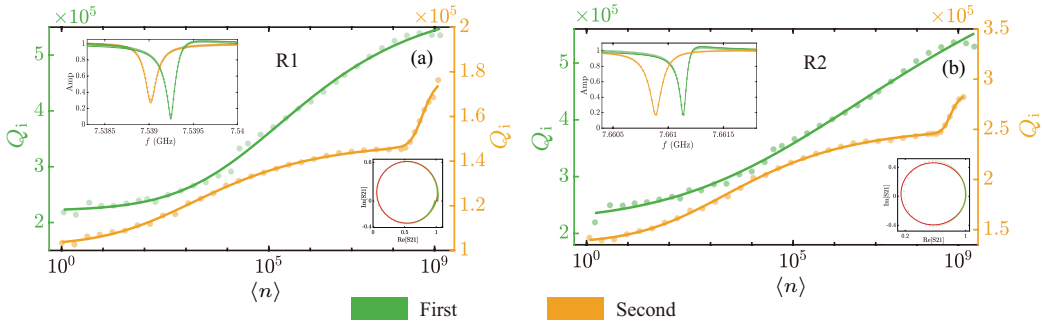

Fig. 2. Characterizations of two resonators. Panels (a) and (b) show the dependence of Q_i on the input photon numbers of R1 and R2, respectively. The upper insets give the typical measured transmission characteristics around the resonant frequencies of resonators below 20 mK, from which Q_i can be deduced by fitting. The bottom insets in panels (a) and (b) show the experimental and fitting data with the maximum input photon numbers in the first measurement of R1 and the second measurement of R2, respectively. Dots (lines) represent the experimental (fitting) results. The green (orange) dots/lines represent the experimental/fitting data in the first (second) measurement.

2.3. Qubit performance

We characterize two transmons[3] with the same structure but different resonant frequencies of the readout resonator. Table 2 gives the parameters of the two transmons. f_r and f_{01} are the resonant frequency of the readout resonator and the transition frequency between the ground and first excited states of the transmon, respectively. f_{02} is the qubit's two-photon transition frequency between the ground and second excited states. E_C and E_J denote the charge and Josephson energies of the transmon, respectively. χ is the dispersive shift. T_1 and T_2 are the energy relaxation time and the spin-echo dephasing time, respectively. We use the pump-and-probe technique[7,11] to measure T_1, as shown typically in the left insets of Figs. 3(a) and 3(c), with the exponential fitting. Long-term monitoring of T_1 is performed (Figs. 3(a) and 3(c)), and the corresponding statistics are analyzed to obtain distributions, which are well fitted by Gaussian functions. The mean value $\overline{T_1}$ of Q1 (Q2) is about 109 μs (95 μs) with the standard deviation of 17.64 μs (6.82 μs). Simultaneously, T_2 of each transmon is measured using a spin-echo sequence and fitted with an exponential function, as shown typically in the left insets of Figs. 3(b) and 3(d). Long-term monitoring of T_2 is also conducted, and the statistical distributions follow Gaussian forms as expected. The mean value $\overline{T_2}$ of Q1 (Q2) is about 22.07 μs (22.32 μs) with the standard deviation of 4 μs (5.21 μs).

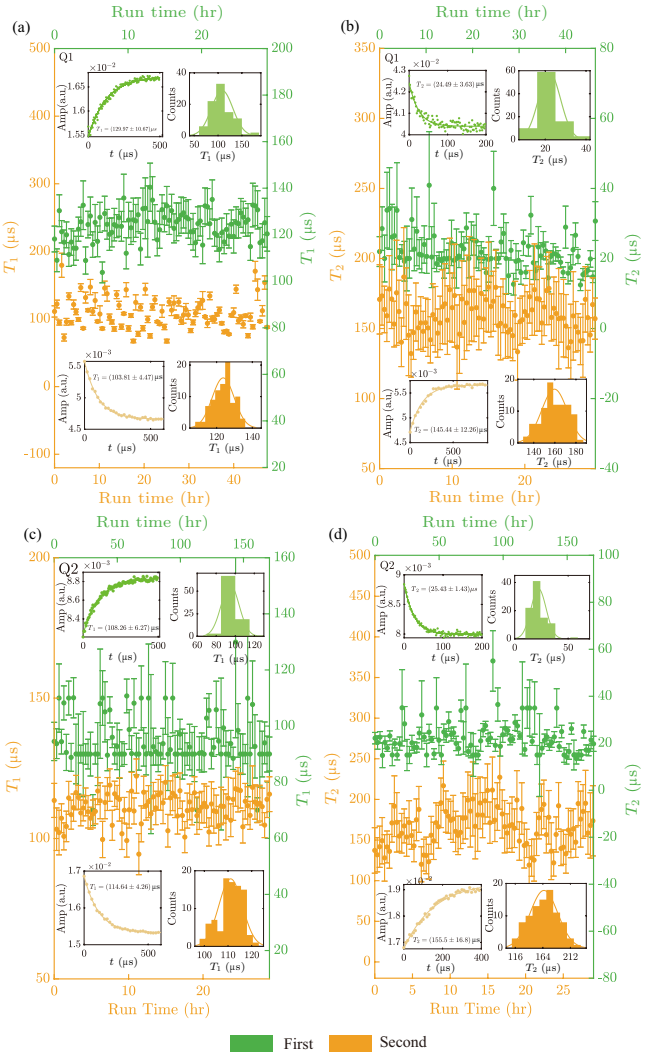

Fig. 3. Long term monitoring of T_1 and T_2 for the two transmon qubits. Panels (a) and (b) are the long-time monitoring of T_1 and T_2 in Q1, respectively. Panels (c) and (d) are the long-time monitoring of T_1 and T_2 in Q2, respectively. The first (second) measured data are represented by the green (yellow) symbols. In each panel, the left inset shows the typical behavior of T_1 or T_2 (dots) with the exponential fitting (line). The right inset displays the corresponding histogram with the Gaussian fitting (line). Note that due to the different readout frequencies of the resonators in two measurements, T_1 and T_2 may increase or decrease exponentially.

Table 2. Parameters of two transmons. Q1 and Q2 represent two transmon qubits, respectively. f_r is the frequency of resonator at which the qubit is read out. f_{01} is the qubit's transition frequency between the ground and first excited states. f_{02} is the qubit's two-photon transition frequency between the ground and second excited states. E_J and E_C are the qubit's Josephson and charge energies, respectively. χ is the dispersive shift. $\overline{T_1}$ ($\overline{T_1'}$) and $\overline{T_2}$ ($\overline{T_2'}$) denote the mean value of the qubit's energy relaxation time and the spin-echo dephasing time in the first (second) measurement, respectively. σ_1 (σ_1') and σ_2 (σ_2') denote the variance of T_1 (T_1') and T_2 (T_2') in first (second) measurement, respectively.

Parameter	Transmon Q1	Transmon Q2
f_r (GHz)	6.196	6.299
f_{01} (GHz)	3.389	3.280
$f_{02}/2$ (GHz)	3.2425	3.1347
E_J/h (GHz)	6.92075	6.5533
E_C/h (GHz)	0.2405	0.2392
χ (MHz)	0.06	0.035
$\overline{T_1} \pm \sigma_1$ (μs)	109±17.64	95±6.82
$\overline{T_1'} \pm \sigma_1'$ (μs)	123.68±6.17	111±4.97
$\overline{T_2} \pm \sigma_2$ (μs)	22.07±4	22.32±5.21
$\overline{T_2'} \pm \sigma_2'$ (μs)	159.64±12.12	165.49±24

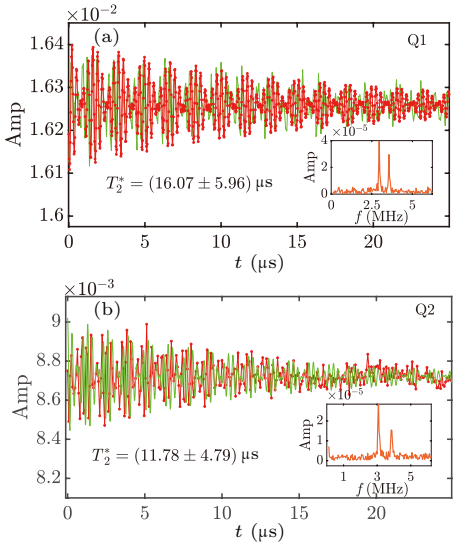

Fig. 4. (a) and (b) The measured Ramsey fringes of two transmon qubits (red dots) fitted by the beating functions (green lines). The insets are the spectra obtained with the Fourier analysis of the experimental data, in which two obvious peaks are observed.

However, as shown in Figs. 4(a) and 4(b), the measured Ramsey fringes present quantum beating, which is distinct from the typical exponentially decaying cosine behavior. Two frequencies are clearly obtained through the Fourier analysis, as shown in the insets. This phenomenon is more pronounced

at higher energy levels,[38–41] which may provide a new platform for studying the properties of low-frequency noise in qubits based on the buffered films. A more detailed discussion about the quantum beating and its effect on the qubit decoherence is given in supplementary information.

2.4. Re-measurement after one year

We measured the sample after one year (referred to as the second measurement) and observed an improvement in the performance of the qubits, especially in T_2, as shown in Fig. 3. $\overline{T_2}$ of Q1 (Q2) is about 159.64 μs (165.49 μs) with a standard deviation of 12.12 μs (24 μs), which is much higher than that in the first measurement. The mixing chamber temperatures are the same, both about 15 mK, during the two measurements. One possible reason for the improvement is that the effective temperature of the sample in the second measurement is somewhat lower than that in the first one, due to the fact that the temperature does not significantly affect the energy relaxation time but has a notable impact on the spin-echo dephasing time.[42] To verify this, we measured the dependence of T_1 and T_2 on the temperature, as shown in Figs. 5(a) and 5(b), in which T_2 decreases more dramatically than T_1 does. Note that in the second measurement, Q_i is lower than that in the first one, as shown in Figs. 2(a) and 2(b). The qubit performance improves despite the reduction of the resonator's, which suggests that the primary factor limiting the decoherence of our sample is not the dielectric loss associated with the resonator. On the other hand, if the low-power quality factor of the resonator affects the coherence time of the qubit greatly, this means that if we increase the quality of the resonator by optimizing the design and fabrication parameters, then we are promisingly expected to have a longer coherence time of the qubit. The effect of the resonator on the coherence time of the qubit is described in detail in supplementary information.

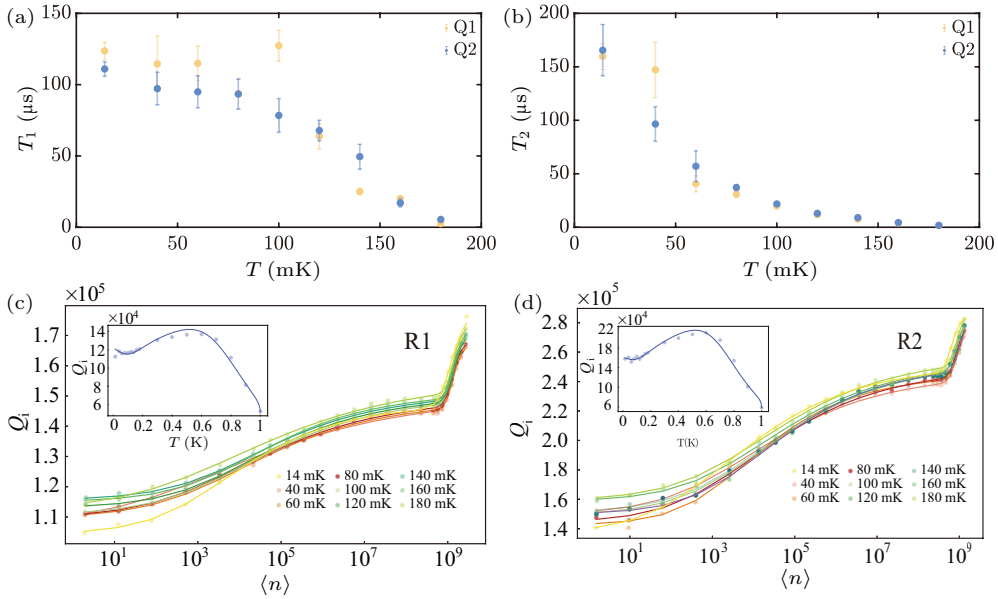

Fig. 5. Panels (a) and (b) are the energy relaxation time T_1 and spin-echo dephasing time T_2 of the two transmon qubits at different temperatures, respectively. Panels (c) and (d) are the variation of Q_i of the two resonators with different input microwave photons at different temperatures. The insets give the dependence of Q_i on the temperature at low power. The dots and solid lines denote the experimental data and the fitting results, respectively.

Another interesting phenomenon, as shown in Figs. 2(a) and 2(b), is the appearance of an "inflection point" in the dependence of Q_i on the input photon numbers, which does not occur in the first measurement. To confirm that the input microwave power is not high enough to make the resonators bifurcate, as examples, the bottom insets in panels (a) and (b) show the experimental and fitting data with the maximum input photon numbers in the first measurement of R1 and the second measurement of R2, respectively. Both of them have not deviated from a circular shape. We measure the dependence of Q_i on the input photon numbers at varied temperatures. The "inflection point" remains almost unchanged, as shown in Figs. 5(c) and 5(d). It is noted that although both T_1 and T_2 decrease to less than 10 μs within the temperature range of our measurements, the "inflection point" in the resonator remains, indicating that the observed effect is not due to the possible temperature difference in the two measurements, but rather to the changes of TLSs of the buffered films. Based on this observation, we divide the resonator losses into those of two layers, which can be fitted as a function of the average number of photons in the resonator using the following expression:

$$\delta_i = \sum_{l=1}^{N} \frac{F\delta_{\mathrm{TLS},0,l}}{\sqrt{1+\left(\frac{\bar{n}}{C_l}\right)^{\beta_l}}} + \delta_{\mathrm{other}}, \tag{3}$$

where l denotes the number of films and $N = 2$ in our experiment. We fit the resonator data using Eq. (3), as shown above, and the results for each dataset are presented in Tables 3 and 4.

Table 3. Fitting parameters of R1 used in Eq. (3) at different temperatures. The errors indicate the standard deviation of the parameter estimation.

T (mK)	$F\delta_{\mathrm{TLS},0,1}$ (10^{-6})	C_1 (10^2)	β_1	$F\delta_{\mathrm{TLS},0,2}$ (10^{-7})	C_2 (10^8)	β_2	δ_{other} (10^{-6})
14	2.79±0.08	2.16±0.45	0.51±0.03	12.67±1.23	3.75±0.23	3.28±0.56	5.51±0.11
40	2.60±0.18	0.55±0.33	0.32±0.03	8.93±0.93	4.81±0.23	5.56±1.29	5.78±0.08
60	2.37±0.07	3.72±0.82	0.42±0.02	8.84±0.70	4.72±0.18	5.46±0.97	5.86±0.06
80	2.42±0.06	3.13±0.65	0.40±0.02	8.73±0.57	4.63±0.15	5.62±0.86	5.82±0.05
100	2.38±0.05	4.89±0.75	0.42±0.02	8.75±0.44	4.37±0.12	5.55±0.68	5.78±0.04
120	2.19±0.08	7.95±2.01	0.45±0.04	9.39±1.17	5.01±0.28	4.98±1.21	5.72±0.10
140	2.03±0.06	9.17±1.71	0.45±0.03	9.30±0.69	4.77±0.17	5.04±0.78	5.69±0.06
160	2.08±0.06	10.37±2.23	0.48±0.03	9.16±0.95	5.11±0.23	5.28±1.12	5.70±0.08
180	2.47±0.11	1.50±0.52	0.34±0.02	8.64±0.70	4.91±0.18	5.53±0.99	5.57±0.06

Table 4. Fitting parameters of R2 used in Eq. (3) at different temperatures. The errors indicate the standard deviation of the parameter estimation.

T (mK)	$F\delta_{\mathrm{TLS},0,1}$ (10^{-6})	C_1 (10^2)	β_1	$F\delta_{\mathrm{TLS},0,2}$ (10^{-7})	C_2 (10^8)	β_2	δ_{other} (10^{-6})
14	3.32±0.07	1.03±0.17	0.48±0.02	5.49±0.59	5.26±0.28	5.47±1.38	3.43±0.05
40	2.60±0.04	4.08±0.50	0.45±0.01	5.73±0.78	7.18±0.36	5.58±1.26	3.50±0.07
60	2.92±0.11	6.17±1.81	0.57±0.05	6.85±5.65	7.96±2.74	4.44±4.19	3.40±0.55
80	2.91±0.08	4.79±1.11	0.47±0.03	5.58±1.75	7.20±0.81	5.68±3.01	3.46±0.16
100	2.75±0.09	7.94±1.93	0.46±0.03	5.09±1.41	6.93±0.70	6.25±3.43	3.43±0.13
120	2.69±0.05	12.93±1.77	0.52±0.02	5.16±1.72	8.28±0.87	6.23±3.03	3.46±0.16
140	2.67±0.07	8.42±1.60	0.47±0.02	5.30±1.26	7.04±0.60	5.92±2.56	3.42±0.12
160	2.36±0.05	10.85±1.67	0.46±0.02	5.56±1.28	7.56±0.62	5.51±1.92	3.38±0.12
180	2.39±0.05	7.99±1.16	0.45±0.02	5.23±0.84	7.24±0.41	6.02±1.73	3.36±0.08

In addition, as shown in the insets of Figs. 5(c) and 5(d), we have also analyzed the performance of the resonators with respect to the temperature in the second measurement. During the measurement of the dependence of Q_{i} on the temperature, a power of about -124 dBm is applied. Because Q_{i} mainly falls within the interval, one can ignore the behavior of Q_{i} that only exhibits at high power. At the same time, we introduce the quasiparticle loss due to the increase of temperature and express the total loss as

$$\delta_{\mathrm{i}} = \sum_{l=1}^{n} (\delta_{\mathrm{TLS},l} + \delta_{\mathrm{QP},l}) + \delta_{\mathrm{other}}, \tag{4}$$

where $\delta_{\mathrm{QP},l}$ denotes the quasiparticle loss of the l-th film layer and can be parametrized by

$$\delta_{\mathrm{QP},l} = \frac{1}{Q_{\mathrm{QP},0,l}} \exp\left(-\frac{\Delta_0}{k_{\mathrm{B}}T}\right)\left[\sinh\left(\frac{hf_{\mathrm{c}}}{2k_{\mathrm{B}}T}\right)\mathrm{K}_0\left(\frac{hf_{\mathrm{c}}}{2k_{\mathrm{B}}T}\right)\right]. \tag{5}$$

Here $Q_{\mathrm{QP},0,l}$ represents the inverse linear absorption from the quasiparticles. Δ_0 is the superconducting gap ($\Delta_0 = 1.764 k_{\mathrm{B}}T_{\mathrm{c}}$). K_0 is the zeroth order modified Bessel function of the second kind.

What is more, the effect of quasiparticles on the buffered resonators during the increase in temperature is consistent with that of a resonator with a single-layer film. The coefficient $\mathrm{e}^{\Delta_0/k_{\mathrm{B}}T}$ of quasiparticle loss for the Nb film with $T_{\mathrm{c}} = 5.09$ K is approximately 40 times larger than that for the Ta film with $T_{\mathrm{c}} = 2.97$ K even at a temperature of 1 K. Therefore, the effect of quasiparticles for the Nb film can be neglected. Thus, we can fit the data with the following equation:

$$\delta_{\mathrm{i}} = \frac{1}{Q_{\mathrm{QP},0}} \exp\left(-\frac{\Delta_0}{k_{\mathrm{B}}T}\right)\left[\sinh\left(\frac{hf_{\mathrm{c}}}{2k_{\mathrm{B}}T}\right)\mathrm{K}_0\left(\frac{hf_{\mathrm{c}}}{2k_{\mathrm{B}}T}\right)\right] + \frac{F\delta_{\mathrm{TLS},0}\tanh\left(\frac{hf_{\mathrm{c}}}{2k_{\mathrm{B}}T}\right)}{\sqrt{1+(A+DT^{\beta_3})^{-1}\tanh\left(\frac{hf_{\mathrm{c}}}{2k_{\mathrm{B}}T}\right)}} + \delta_{\mathrm{other}}. \tag{6}$$

Because we have obtained $F\delta_{\mathrm{TLS},0}$ and δ_{other} by fitting Q_{i} as a function of photon numbers, there are only four free-fitting parameters: *i.e.*, A, D, β_3, and $Q_{\mathrm{QP},0}$. Table 5 lists the fitting parameters. The fitting results are shown in the insets of Figs. 5(c) and 5(d). Q_{i} has different behaviors in three temperature regimes. When the temperature is below about 180 mK, Q_{i} decreases slightly as the temperature increases due to the decreasing coherence time of the TLS. When the temperature is higher than about 600 mK, where the ratio of temperature to T_{c} is much higher, the effect of quasiparticle loss causes Q_{i} to decrease exponentially with the temperature. From 180 mK to 600 mK, Q_{i} increases slightly with the temperature, consistent with the gradual saturation of TLSs. These results are consistent with those reported previously.[24,25]

Table 5. Fitting parameters of resonators used in Eq. (6) for different temperatures at low input microwave power. The errors indicate the standard deviation of the parameter estimation.

Resonator	f_{c} (GHz)	A	D	β_3	$Q_{\mathrm{QP},0}$
R1	7.5393	1.02±0.85	–1.2±0.85	–0.43±0.21	205.31±11.92
R2	7.6612	3.21±6.01	–3.40±6.01	–0.35±0.45	204.88±10.73

To further analyze the "inflection point" quantitatively, we fix β_1, C_1, $F\delta_{\mathrm{TLS},0,1}$, and δ_{other}, and vary β_2, C_2, and $F\delta_{\mathrm{TLS},0,2}$ in Eq. (3). As shown in Fig. 6, β_2 and $F\delta_{\mathrm{TLS},0,2}$ only affect the shape of Q_{i} with respect to the input photon numbers, while C_2 determines the position of the "inflection point",

where C_2 is equal to the input photon number as marked by the pentagram in Fig. 6. Because C_2 is related to the coherence time of TLSs in the film, the appearance of the "inflection point" suggests that the conditions of the TLSs may have changed. Note that the difference between the two measurements is not only the two layers but also the oxidation of the surfaces and interfaces between the two layers. The change of TLSs in one of the two layers is one possible reason. Further investigation, such as more samples with different parameters in the film deposition and more characterizing methods such as TEM with EDS, is required to find out other possible reasons which may result in the "inflection point".

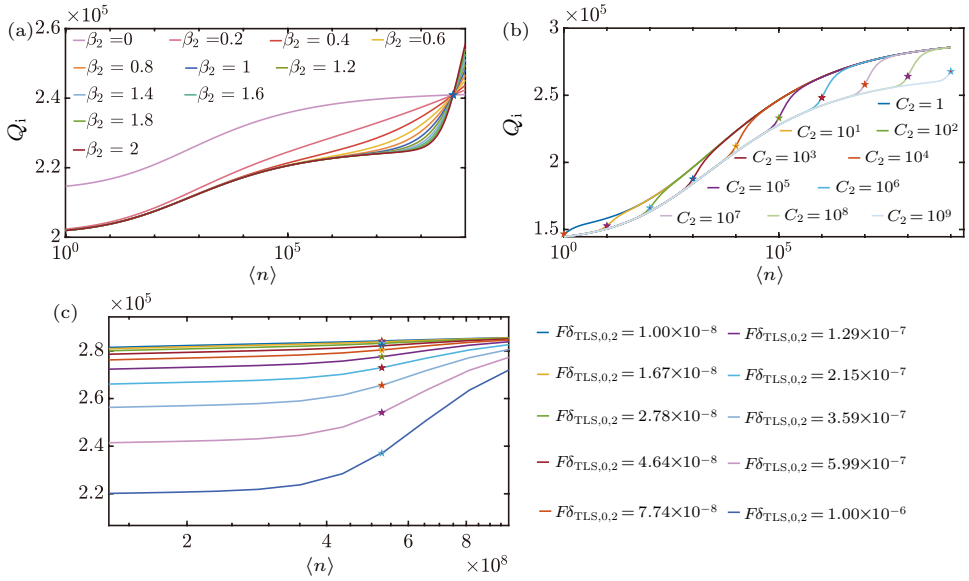

Fig. 6. The dependence of Q_i on the input photon numbers is calculated with different (a) β_2, (b) C_2, and (c) $F\delta_{\mathrm{TLS},0,2}$. The pentagram in each figure indicates the position where the photon number is equal to C_2.

3. Conclusion

In summary, we deposited the tantalum film with Nb as the buffer layer on the sapphire substrate at room temperature. The observed performance demonstrates the successful achievement of α-Ta with high quality. Although the internal quality factor of resonators based on this buffered superconducting film and the critical temperature of the films do not reach the best levels reported in other studies, the superconducting transmon qubits based on the buffered film exhibit excellent performance. With further optimization of the fabrication process and parameters (*e.g.*, increasing the critical temperature of the buffered films and designing qubits with larger E_J/E_C ratios), we are optimistic that the performance of these qubits can be further enhanced. These buffered films hold significant promise for applications where high deposition temperatures are strictly prohibited. Measurement of the sample a year apart reveals an "inflection point" in the internal quality factor of the resonator. This is possibly attributed to the changes of TLSs in the two films, which offers insights into the degradation mechanisms of these buffered films for applications in quantum and/or classical devices.

Acknowledgements

Project supported by Quantum Science and Technology–National Science and Technology Major Project of China (Grant No. 2021ZD0301701), the National Natural Science Foundation of China (Grant No. 62288101), the Fund from State Key Laboratory for Novel Software Technology at Nanjing University, the Dengfeng Project of Nanjing University, and the Fund from Ministry of Education Engineering Research Center for Optoelectronic Materials and Chip Technology.

References

[1] Nguyen L B, Lin Y H, Somoroff A, Mencia R, Grabon N and Manucharyan V E 2019 *Phys. Rev. X* **9** 041041

[2] Somoroff A, Ficheux Q, Mencia R A, Xiong H, Kuzmin R and Manucharyan V E 2023 *Phys. Rev. Lett.* **130** 267001

[3] Koch J, Terri M Y, Gambetta J, Houck A A, Schuster D I, Majer J, Blais A, Devoret M H, Girvin S M and Schoelkopf R J 2007 *Phys. Rev. A* **76** 042319

[4] Gambetta J M, Murray C E, Fung Y K K, McClure D T, Dial O, Shanks W, Sleight J W and Steffen M 2016 *IEEE Trans. Appl. Supercond.* **27** 1700205

[5] Nersisyan A, Poletto S, Alidoust N, Manenti R, Renzas R, Bui C V, Vu K, Whyland T, Mohan Y, Sete E A, Bestwick A, Didier N and Houck A 2019 *IEEE International Electron Devices Meeting (IEDM)* December 7–11, 2019, San Francisco, USA pp. 31.1–31.1.4

[6] Paik H, Schuster D I, Bishop L S, Kirchmair G, Catelani G, Sears A P, Johnson B R, Reagor M J, Frunzio L, Glazman L I, Girvin S M, Devoret M H and Schoelkopf R J 2011 *Phys. Rev. Lett.* **107** 240501

[7] Jiang J L, Li Z S, Guo T T, Xu W Q, Wei X Y, Zhang K X, Zhou T S, Sheng Y F, Cao C H, Sun G Z and Wu P H 2022 *Appl. Phys. Lett.* **121** 254001

[8] Chang J B, Vissers M R, Córcoles A D, Sandberg M, Gao J, Abraham D W, Chow J M, Gambetta J M, Rothwell M B, Keefe G A, Steffen M, McDermott R and Pappas D P 2013 *Appl. Phys. Lett.* **103** 012602

[9] Kim S, Terai H, Yamashita T, Qiu W, Fuse T, Yoshihara F, Ashhab S, Inomata K and Semba K 2021 *Commun. Mater.* **2** 98

[10] Samkharadze N, Bruno A, Scarlino P, Zheng G, DiVincenzo D, DiCarlo L and Vandersypen L 2016 *Phys. Rev. Appl.* **5** 044004

[11] Wei X Y, Jiang J L, Xu W Q, Guo T T, Zhang K X, Li Z S, Zhou T S, Sheng Y F, Cao C H, Sun G Z and Wu P H 2023 *Appl. Phys. Lett.* **123** 154005

[12] Place A P, Rodgers L V, Mundada P, *et al.* 2021 *Nat. Commun.* **12** 1779

[13] Place A P M 2022 *Increasing Lifetimes of Superconducting Qubits*, Ph. D. Dissertation (Princeton: Princeton University)

[14] Wang C, Li X, Xu H, Li Z, Wang J, Yang Z and Yu H 2022 *npj Quantum Inf.* **8** 3

[15] Siddiqi I 2021 *Nat. Rev. Mater.* **6** 875

[16] Geerlings K L 2013 *Improving coherence of superconducting qubits and resonators*, Ph. D. Dissertation (New Haven: Yale University)

[17] Latif R, Jaafar M F, Aziz M F, Zain A R M, Yunas J and Majlis B Y 2020 *Int. J. Refract. Met. Hard Mater.* **92** 105314

[18] Huang M, Liu Y S, He Z B and Yi Y 2022 *Chin. Phys. B* **31** 066101

[19] Hallmann L and Ulmer P 2013 *Appl. Surf. Sci.* **282** 1

[20] Ferreira F, Cavaleiro A and Oliveira J 2020 *Metals* **10** 1618

[21] Cho M G, Kang U, Lim S H and Han S 2023 *Thin Solid Films* **767** 139668

[22] Chen W C, Wang Z Y, Yu C Y, Liao B H and Lin M T 2022 *Surf. Coat. Technol.* **436** 128288

[23] Shi L, Guo T, Su R, Chi T, Sheng Y, Jiang J, Cao C, Wu J, Tu X, Sun G, Chen J and Wu P 2022 *Appl. Phys. Lett.* **121** 242601

[24] Crowley K D, McLellan R A, Dutta A, Shumiya N, Place A P M, Le X, Gang Y, Madhavan T, Khedkar N, Feng Y C, *et al.* 2023 *Phys. Rev. X* **13** 041005

[25] Urade Y, Yakushiji K, Tsujimoto M, Yamada T, Makise K, Mizubayashi W and Inomata K 2024 *APL Mater.* **12** 021132

[26] Face D W and Prober D E 1987 *J. Vac. Sci. Technol. A* **5** 3408

[27] Li D, Hu J, Li Y and An S 2024 arXiv preprint arXiv: 2405.02955 [quant-ph]

[28] Li Z S, Guo T T, Xu W Q, Shi L L, Zhang K X, Zuo Q, Zhou T S, Sun G Z and Wu P H 2025 *Mater. Res. Express* **12** 026001

[29] Bu K, Zong Z, Zhang Z, Ma X, Shao M, Li D, Li Y, Hu J, Huai S, An S, Cai T, Yang X, Dai M, Zheng Y C and Zhang S 2025 *Supercond. Sci. Technol.* **38** 035010

[30] Fan Y, Liu Y, Liu Y, Peng W, Wu Y, Mu G and Lin Z R 2025 *Physica C* 1354652

[31] Navid A A and Hodge A M 2012 *Mater. Sci. Eng. A* **536** 49

[32] Deng H, Song Z, Gao R, Xia T, Bao F, Jiang X, Ku H-S, Li Z, Ma X, Qin J, *et al.* 2022 arXiv preprint arXiv: 2205.03528 [quant-ph]

[33] Khalil M S, Stoutimore M J A, Wellstood F C and Osborn K D 2012 *J. Appl. Phys.* **111** 054510

[34] Probst S, Song F, Bushev P A, Ustinov A V and Weides M 2015 *Rev. Sci. Instrum.* **86** 024706

[35] Gao J 2008 *The physics of superconducting microwave resonators*, Ph. D. Dissertation (Pasadena: California Institute of Technology)

[36] Goetz J, Deppe F, Haeberlein M, Wulschner F, Zollitsch C W, Meier S, Fischer M, Eder P, Xie E, Fedorov K G, Marx A, Gross R and Huebl H 2016 *J. Appl. Phys.* **119** 015304

[37] Arzeo M, Lombardi F and Bauch T 2014 *Appl. Phys. Lett.* **104** 212601

[38] Tennant D M, Martinez L A, Beck K M, O'Kelley S R, Wilen C D, McDermott R, DuBois J L and Rosen Y J 2022 *PRX Quantum* **3** 030307

[39] Burnett J, Bengtsson A, Scigliuzzo M, Niepce D, Kudra M, Delsing P and Bylander J 2019 *npj Quantum Inf.* **5** 54

[40] Martinez L, Peng Z, Appel D, Tennant D, Petersson N A, DuBois J L and Rosen Y J 2023 *Appl. Phys. Lett.* **122** 114002

[41] Peterer M J, Bader S J, Jin X, Yan F, Kamal A, Gudmundsen T J, Leek P J, Orlando T P, Oliver W D and Gustavsson S 2015 *Phys. Rev. Lett.* **114** 010501

[42] Murray C E 2021 *Mater. Sci. Eng. R* **146** 100646